Journal of Applied Fluid Mechanics, Vol. 18, No. 4, pp. 864-879, 2025.
Available online at www.jafmonline.net, ISSN 1735-3572, EISSN 1735-3645.
https://doi.org/10.47176/jafm.18.4.2980

Study on the LES of Premixed Gas Flame Dynamics in a Weak Confinement Structure: The Influence of Continuous Obstacle Plates

X. Shao [1], J. Gao [1,2,3†], B. Hao[4], B. Ai[1], Y. Han[1], Y. Wu[1] and B. Guo[1]

[1] *School of Petrochemical Engineering & Environment, Zhejiang Ocean University, Zhoushan, 316022, China*
[2]*National & Local Joint Engineering Research Center of Harbor Oil & Gas Storage and Transportation Technology, Zhoushan 316022, China*
[3]*Zhejiang Key Laboratory of Petrochemical Environmental Pollution Control, Zhejiang Ocean University, Zhoushan 316022, China*
[4]*Sinochem Zhoushan Hazardous Chemicals Emergency Rescue Base CO., LTD., Zhoushan 316021, China*

†*Corresponding Author Email: gaojf409@zjou.edu.cn*

ABSTRACT

The layout of equipment and structures in underground utility tunnels has a significant impact on the safety of spaces. In this paper, experimental and simulation methods are combined to investigate the detonation characteristics of propane(C_3H_8)-air mixtures. By placing continuous obstacle plate at different positions within a pipeline, we examine the flame behavior, pressure, and flow field during the detonation process. The findings reveal that continuous obstacles create greater disturbances than single obstacles. When continuous obstacles are placed 500 mm and 800 mm from the ignition point, a secondary reignition phenomenon occurs; however, there is little difference in the time it takes for the flame front to reach the pipe's outlet. Additionally, when continuous obstacles are positioned 200 mm and 800 mm from the ignition point, the detonation reaction weakens, with pressure peak reductions of 8.57% and 3.98% compared to the case with three single obstacles, and the maximum flame area decreases by 6.60% and 2.19%. In contrast, placing obstacles at 500 mm heightens the detonation reaction, resulting in a 2.92% increase in the pressure peak and a 19.87% increase in the maximum flame area compared to the case with three single obstacles.

Article History

Received July 15, 2024
Revised October 7, 2024
Accepted October 20, 2024
Available online February 4, 2025

Keywords:

Experimental study
Explosion behavior
Numerical simulation
Obstacle disturbance
Propane-air mixtures

1. INTRODUCTION

In recent years, with the development of underground utility tunnels (Liu et al., 2024), municipal pipelines for various purposes have been centrally managed, connecting the entire city through these spaces. The transportation of flammable and explosive materials, such as petroleum and natural gas (Bu et al., 2021), necessitates effective safety measures. Safety issues in underground utility tunnels have become a focal point in related research. The gases transported in urban underground utility tunnels are often used as energy supplies. These gases, characterized by high calorific values and flammability, can significantly impact potential leakage and deflagration events. Gases such as methane, propane, and hydrogen have been the focus of significant academic research. Scholars have analyzed the explosive limits of these gases (Cui et al., 2016; Shen et al., 2017; Huang et al., 2019; Li et al., 2019; Huang et al., 2021, 2022) and their deflagration characteristics at different concentrations (Bao et al., 2016; Ajrash et al., 2017; Chen et al., 2020; Saeid et al., 2021; Huo et al., 2022; Wang et al., 2022). Saeid et al. (2021) studied the detonation characteristics of homogeneous and heterogeneous mixtures with hydrogen concentrations of 15% and 30% in pipelines containing obstacles. They found that at relatively low hydrogen concentrations, detonation only occurred in heterogeneous mixtures, typically within the normal sections of the channel. When the hydrogen concentration was increased to 30%, detonations were observed in both homogeneous and heterogeneous mixtures in the obstructed sections of the channel. The flame front in the homogeneous mixtures propagated symmetrically, while in the heterogeneous mixtures, it was asymmetrical and usually occurred in the upper regions of the channel. Additionally, Debnath and Pandey (2024) compared the performances of stoichiometric hydrogen-air and kerosene-air fuels (φ=1) and found that the hydrogen-air mixtures had a higher exergetic efficiency than the kerosene-air mixtures.

NOMENCLATURE

ρ	density	T	temperature
t	time	D	diffusion coefficient
u	speed	$\dot{\omega}_c$	normalized chemical reaction rate
p	pressure	S	heat of chemical reaction
τ_{ij}	viscous stress tensor	H	calorific value
u_i	velocity component	μ_{sgs}	subgrid viscosity coefficient
u_j	velocity component	L_s	subgrid-scale mixing length
h	enthalpy	s_{ij}	spin rate tensor component
λ	thermal conductivity		

Different geographic environments result in varying capacities and lengths of underground utility tunnel spaces. Many scholars have established physical models with different length to diameter ratios for experiments and have observed some interesting phenomena. For instance, Hong et al. (2016) studied the deflagration behavior characteristics of closed and open pipes of different widths and found that the geometric shape of the pipe influences the evolution of the deflagration behavior. In closed pipes, as the length/diameter ratio increases, the peak pressure increases, and as the length/diameter ratio decreases, the pressure peak decreases. In open pipes, the flame speed increases as the propagation distance increases. Additionally, the leakage and deflagration positions within underground utility tunnel spaces are complex. Many scholars have explored different explosion ignition positions. Wan et al. (2023) found that the ignition position affects the flame structure of premixed PO/air mixtures. At the starting point, the flame gradually evolves from spherical to elliptical to tulip-shaped, while at ignition positions farther from starting point, the flame expands directly from spherical to finger-like and spreads sideways upon touching the walls. The overpressure peak decreases as the ignition position moves farther away.

Due to structural needs, underground utility tunnel spaces often contain various barriers. After a leak-induced explosion in a gas pipeline, these obstacles disturb the flame's behavior and the overpressure characteristics generated by the explosion, affecting the consequences of the incident. In recent years, numerous scholars have constructed simplified spatial physical models, in which various types of obstacles are placed, to simulate deflagration flame behavior under obstacle disturbance through experimental and numerical simulation methods. These studies aimed to investigate the potential impact of the deflagration behavior under different conditions in underground utility tunnel spaces.

Some researchers have investigated the variations in explosion fluctuations by modifying the number or position of obstacles. For example, Qin and Chen (2021) studied the relationship between obstacles and the flame behavior in a pipeline after deflagration. They found that obstacles disturb the flame during its propagation, causing deformation and distortion as it passes each obstacle, which increases the intensity of the turbulence. They pointed out that the flame structure exhibits typical self-similarity and proposed the concept of the fractal dimension, with more obstacles leading to more fragmented flames and larger resultant fractal dimensions. Additionally, Lv et al. (2016) investigated the influence of the obstacle position on the detonation behavior in semi-enclosed areas. They found that an increase in the number of obstacles led to a higher overpressure peak, and the maximum peak pressure was located downstream of the most distant obstacle. However, more obstacles do not always monotonically increase the overpressure peak. Na'inna et al. (2015) discovered that for three obstacles, the explosion peak pressure is highest when the spacing between the last two obstacles corresponds to the optimal spacing between the first two obstacles. This indicates that denser obstacle groups do not necessarily result in more severe explosions. Optimal spacing of not too crowded obstacles can result in a higher peak overpressure.

Moreover, some scholars have explored the shapes of obstacles and have discovered that different shapes significantly impact the flame behavior and overpressure characteristics of explosions. For instance, Liu et al. (2023) found that in pipelines containing triangular obstacles, the deflagration to detonation transition time is shorter due to the enhanced flame-vortex interactions enabled by the inclined surfaces of the triangular obstacles. However, when the blockage ratio increases, the obstacle's shape loses its significant influence on the flame (Mei et al., 2023). Many scholars have studied the blockage ratio of obstacles (Debnath et al., 2014) and have identified unique relationships between changes in the blockage ratio and the flame behavior and overpressure during deflagration. Mei et al. (2023) discovered that single obstacles have a higher sensitivity to the blockage ratio and overpressure growth rate than grid-like obstacles. The flames are slightly suppressed by the reflected waves at the front of the obstacles, and the suppression effect becomes more pronounced as the blockage ratio increases. Debnath et al. (2023) studied the effect of the blockage ratio on detonation wave propagation and flame acceleration characteristics and found that the flame acceleration is most pronounced for a blockage ratio of 0.39 for stoichiometric (φ=1) fuel-air mixtures. Further research has demonstrated that changes in the blockage ratio significantly affect the temperature, turbulent viscosity, flame speed, and pressure during the detonation process. While many scholars have examined the impact of different obstacles on the detonation behavior within pipelines, most studies simplified the shapes to basic forms when few addressing flame behavior and pressure propagation characteristics in densely packed structures and equipment by controlling the shapes of the obstacles.

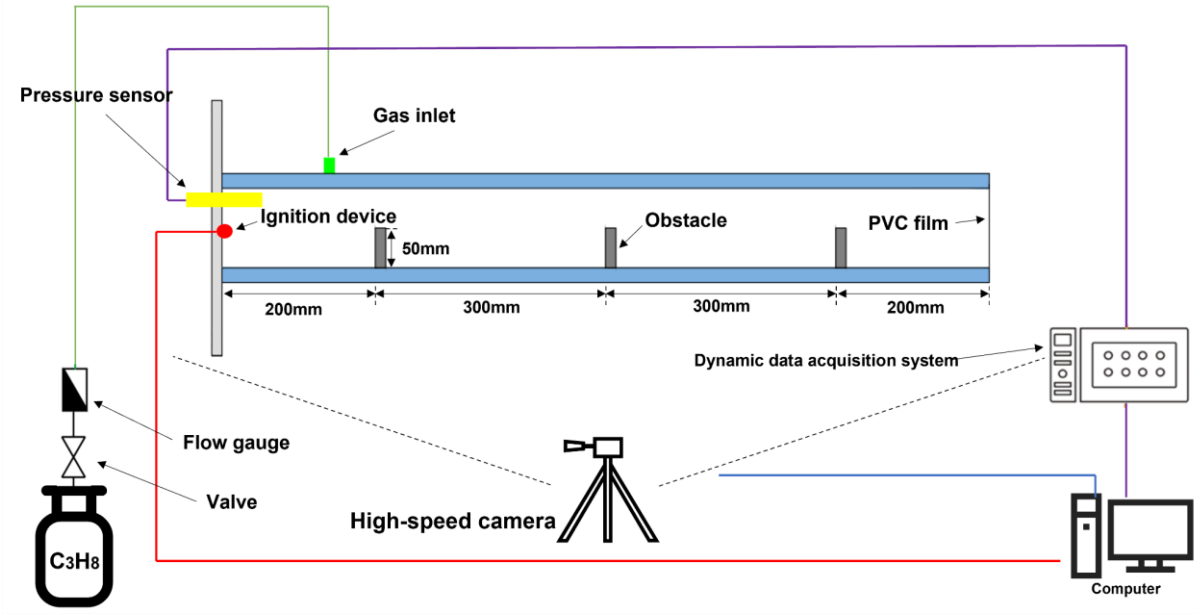

Fig. 1 Diagram of experimental equipment

Therefore, in this study, we simulated the detonation behavior following a propane leak in a utility tunnel by constructing continuous obstacles with a blockage ratio of 50% and single obstacles. The arrangement of continuous obstacles was adjusted at distances of 200 mm to 800 mm from the ignition point within the pipeline. An experimental system was established to validate the validity of the simulation settings, followed by analysis of the unique characteristics of flame propagation at different continuous obstacle placements and their impact on the flame behavior within the pipeline. The aims of this study were to analyze the detonation process under different conditions and to determine the flame behavior and detonation mechanisms in pipelines containing continuous obstacles, with a focus on changes in the pressure values, flame behavior, velocity, and flow field. This will provide theoretical guidance for the design of utility tunnels with densely placed equipment and structures, reducing the risk of propane gas leak explosions in such environments.

2. EXPERIMENTAL STEPS

2.1 Experimental Platform

Figure 1 shows the instruments we used. The pipeline had a volume of 0.01 m^3 and internal dimensions of 100 mm x 100 mm x 1000 mm. This pipeline was constructed of 5 mm thick Q235-A steel plates, and a 20 mm thick high-strength explosion-proof organic glass plate was located on the front. The plates were connected by screws. On the left side of the pipeline, there was an electric spark ignition device (KTGD-B type adjustable ignition device) with an energy range of 0.5 to 20 J. A pressure sensor was located 30 mm above the ignition. This sensor had a range of 0–5 MPa and a high measurement accuracy. The obstacles inside the pipeline were connected through two Φ = 20 mm internal threaded holes. The open end of the right side of the pipe was sealed with PVC film before filling, which had minimal impact on the internal flow field during deflagration and was almost negligible. To ensure the sealing of the reaction chamber, 2 mm thick soft rubber strips were placed at the joints, and foam water was sprayed after each disassembly and assembly to check the airtightness of the reaction chamber. This reaction chamber could withstand pressures of 0–3 MPa, fully meeting the standards of this experiment.

Figure 2 presents a three-dimensional dimensional map of the two obstacles we used. A combination of three veneers with dimensions of 100 mm x 50 mm x 5 mm were welded with the same material and pipe wall was consistent with the Q235-A type steel plate cutting and welding production. The bottom end was fixed by bolts inside the pipe.

A camera recording at 960 fps was used to document the flame behavior inside the reaction pipeline from the front. The captured flame images and pressure signals were saved by the data acquisition system. To ensure thorough premixing of the gas in the reaction pipeline, an external gas recirculation pump was used to promote gas flow inside the pipeline. After each set of experiments, an air gun was used to flush the inside of the pipeline to avoid residual exhaust gas affecting the next experiment.

2.2 Experimental Methods

In this study, we utilized a stoichiometric (ϕ=1) propane-air mixture in the detonation experiments. Once the equipment connections were completed, the pressure relief valve on the propane tank was opened to release the propane gas. The flow rate of the propane through the hose was controlled at 0.3 L/min using a flow controller. After inflating the gas inlet for 80.6 seconds, the inlet was closed. The gas circulation pump was operated for 3 minutes to ensure uniform gas mixing in the pipeline. Subsequently, the gas circulation pump was removed, and the high-speed camera was activated before the start of the ignition. This procedure was repeated three times to ensure experimental validity.

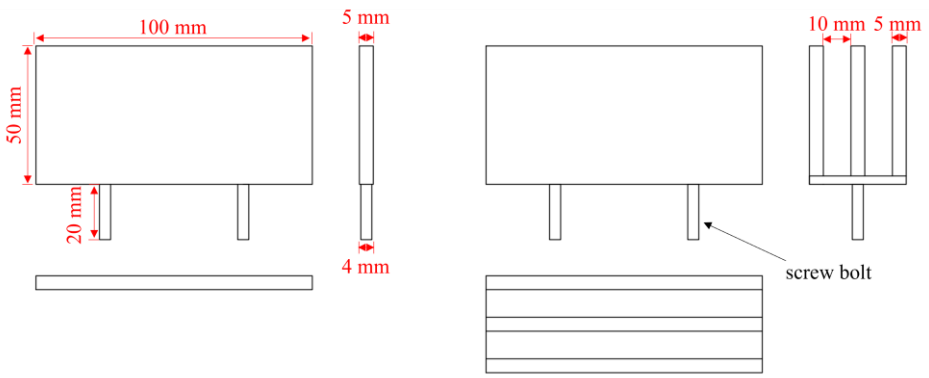

(a) single plate obstacles (b) Continuous Obstacle Plate

Fig. 2 Three-dimensional schematic diagram of the single plate obstacles and continuous obstacle plate

3. NUMERICAL MODEL

3.1 Theoretical Basis

In order to observe the flame development trend and flow field of the propane-air premixed explosion, we used Fluent to replicate the experiment.

In this study, we employed large eddy simulation (LES) and a premixed combustion model to conduct numerical simulations. Compared to direct numerical simulation methods, LES only simulates large structures, and small structures are approximated using subgrid models, saving considerable computational resources. Additionally, LES can more accurately describe vortices and other complex flow regions compared to Reynolds-averaged Navier-Stokes (RANS) models. Many researchers have used LES to investigate premixed combustion processes and have demonstrated the reliability of this method (Liu & Wang 2022; Pan et al., 2022). The for mass, momentum, energy, and species conservation equations, coupled with constitutive equations and state equations, yield the following LES control equations:

$$\frac{\partial \rho}{\partial t}+\frac{\partial\left(\rho \tilde{u}_j\right)}{\partial x_j}=0, \tag{1}$$

$$\frac{\partial\left(\rho \tilde{u}_j\right)}{\partial t}+\frac{\partial\left(\rho \tilde{u}_i \tilde{u}_j\right)}{\partial x_j}=\frac{\partial \sigma_{ij}}{\partial x_i}-\frac{\partial \bar{p}}{\partial x_i}-\frac{\partial \tau_{ij}}{\partial x_j}, \tag{2}$$

$$\frac{\partial\left(\rho \tilde{h}_s\right)}{\partial t}+\frac{\partial\left(\rho \tilde{u}_i \tilde{h}_s\right)}{\partial x_i}-\frac{\partial \bar{p}}{\partial t}-\bar{u}_j \frac{\partial \bar{p}}{\partial x_i}$$
$$-\frac{\partial}{\partial x_i}\left(\lambda \frac{\partial \tilde{T}}{\partial x_i}\right)=-\frac{\partial}{\partial x_j}\left[\rho\left(u_i \tilde{h}_s-\tilde{u}_i \tilde{h}_S\right)\right], \tag{3}$$

where T is temperature. u_i and u_j are velocity components, h is enthalpy, λ is the thermal conductivity, and τ_{ij} is the viscous stress tensor. The transport equation for the Favre-filtered reaction progress variable c is as follows:

$$\frac{\partial(\rho \tilde{c})}{\partial t}+\nabla \cdot(\rho \tilde{u} \tilde{c})+\nabla[\rho(\widetilde{uc}-\tilde{u} \tilde{c})]=\overline{\nabla \cdot(\rho D \nabla \tilde{c})}+\overline{\dot{\omega}_c}, \tag{4}$$

where D is the diffusion coefficient. $\dot{\omega}_c$ is the normalized chemical reaction rate, which is derived using the equation $\dot{\omega}_c=\frac{S}{HY_{fuel}}$, where Y_{fuel} is the mass fraction of fuel in the mixture, and S is the heat of reaction H is the heating value. The tilde symbol denotes Favre-filtered quantities, while the minus symbol indicates physical space filtering.

To close the equations, a subgrid model was established. We employed the Wall-adapting Local Eddy-Viscosity (WALE) model, which effectively captures the transition from laminar to turbulent flow and has a relatively low computational cost (Nicoud & Ducros, 1999).

$$\tau_{ij}-\frac{1}{3}\tau_{kk}\delta_{ij}=-2\mu_{sgs}\bar{s}_{ij}. \tag{5}$$

In Equation (5), μ_{sgs} is the subgrid viscosity coefficient:

$$\mu_{sgs}=\rho L_s^2\frac{\left(s_{ij}s_{ij}\right)^{3/2}}{\left(\bar{s}_{ij}\bar{s}_{ij}\right)^{3/2}+\left(s_{ij}s_{ij}\right)^{5/4}}, \tag{6}$$

Where s_{ij} is the spin rate tensor component, and L_s is the subgrid scale mixing length. We used the Zimont combustion model (Zimont & Battaglia 2006) to thicken the flame, and the turbulent flame was calculated as follows:

$$u_t=A(u')^{\frac{3}{4}}U_l^{\frac{1}{2}}\alpha^{-\frac{1}{4}}l_t^{\frac{1}{4}}, \tag{7}$$

where A is the model constant, which is equal to 0.5. $u'$is the mean-square velocity; U_l is the laminar flame velocity; α is the molar heat transfer coefficient of the unburned mixture; and l_t is the turbulence length scale.

3.2 Grids and Initial Conditions

In the numerical simulation, we selected the internal space of the pipe as the computational domain, and the computational domain was consistent with the effective internal size of the pipe (100 mm x 100 mm x 1000 mm).

Figure 3 shows the result of the grid drawn using the ANSYS ICEM CFD software. For this regular geometric structure, using a hexahedral mesh is most appropriate. The grid quality in Fig. 3 is excellent, and the grid nodes

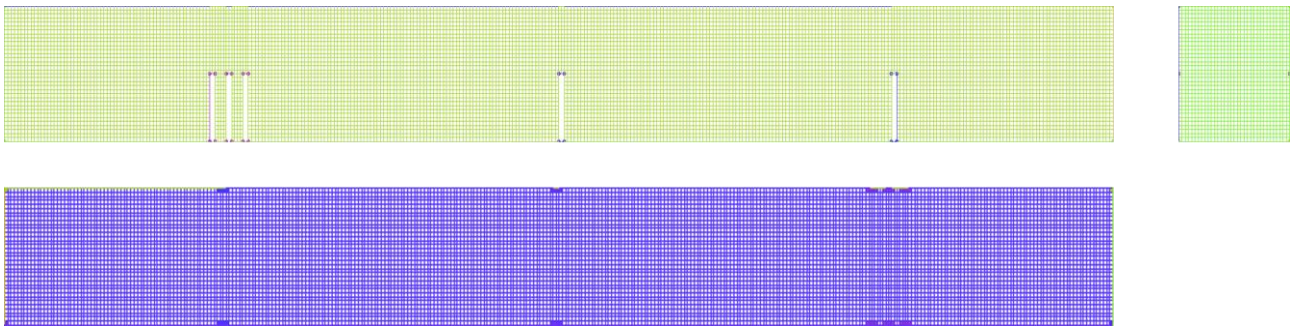

Fig. 3 Simulation Grid Diagram

Table 1 Grouping of cases

Case	Distance (mm)		
	200	500	800
Case 1	single piece	single piece	single piece
Case 2	continuous plate	single piece	single piece
Case 3	single piece	continuous plate	single piece
Case 4	single piece	single piece	continuous plate

Table 2 Parameter Settings for tube

Parameters	Value	Parameters	Value
Thermal Conductivity (W/(m K))	0.024	Molecular Weight (kg/kmol)	29.4652
Laminar Flame Speed (m/s)	0.36	Heat of Combustion (J/kg)	5.0329×10^{7}
Unburnt Fuel Mass Fraction	0.0603		

are connected throughout the computational domain.

Four sets of operating conditions were set in the simulation (Table 1). The horizontal axis numbers represent the distance between the obstacle layout points and the firestarter.

3.3 Boundary Conditions and Parameter Details

The walls of the pipeline were set as WALL, with no-slip and adiabatic characteristics, and the outer walls of the embedded obstacles were also set as WALL. The rightmost outlet of the pipeline was designated as a pressure outlet with a non-reflective characteristic. The internal temperature inside was set to 300 K. The SIMPLE algorithm (Patankar, 1980) was used to solve the model by iteratively determining the velocity and pressure fields through prediction and correction steps. A second-order windward format and a premixed combustion model were chosen for the simulations. We used the reaction progress variable c to describe the flame front, where c=0 indicates unburned fresh mixture gas and c=1 denotes the products of complete combustion. A 5 mm diameter sphere was set at the ignition point as the initial ignition source.

Table 2 presents the propane physical property parameters set in the solver. The laminar flame speeds have been studied for propane (Metghalchi & Keck, 1980). The time step was set to $1\text{x}10^{-6}$ s, and each time step required 40 iterations. In the running residual criterion, except for the energy and process variables, all of the other items were set to $5e^{-5}$.

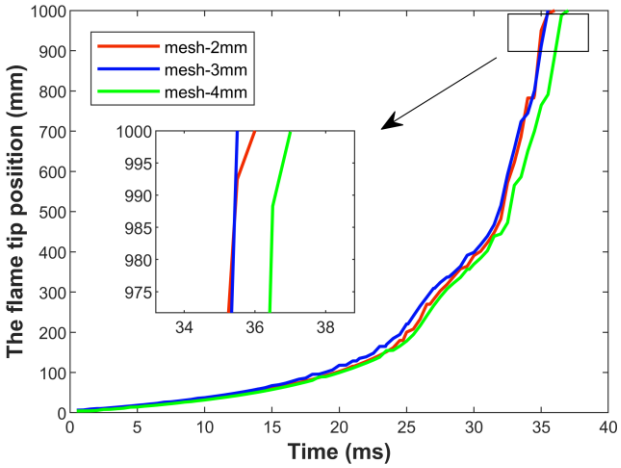

Fig. 4 Grid independence test of computational domain

3.4 Grid Independent Verification

Figure 4 compares the simulation data for three grid sizes. In this study, we conducted a grid independence test by setting global grid sizes of 2 mm, 3 mm, and 4 mm.

The accurate simulations of the variation in the position of the flame front for all three global grid sizes used in this study are shown in Fig. 4. As the global grid size decreased, the accuracy of the solution increased, and the position of the flame front became closer to the experimental data. When the global grid size was less than or equal to 3 mm, the position of the flame front

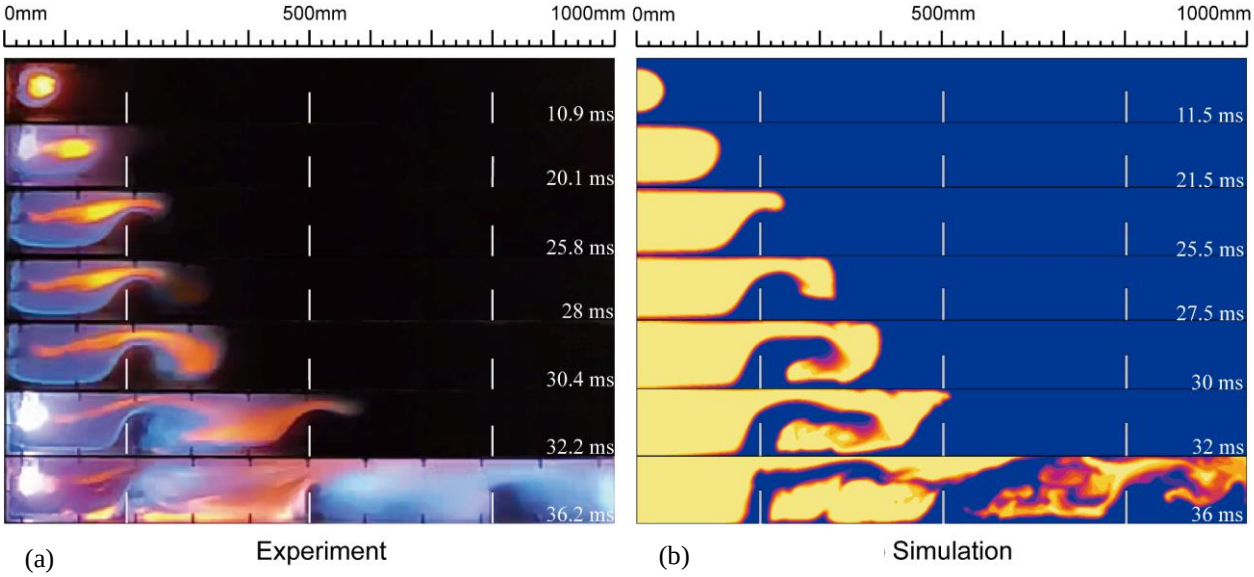

Fig. 5 Trend of flame development

almost no longer changes. Considering the limited computational resources and the validity of the data, all of the grid models in this study had a grid size of 3 mm x 3 mm x 3 mm.

3.5 Validation of the Validity of the Numerical Simulations

Figure 5 compares the flame images obtained using a high-speed camera with the simulated flame images. It can be seen from Fig. 5(b) that the model accurately reproduced the deflagration process inside the pipeline under the real conditions, and the trend was similar to the actual flame trend in the pipeline. After the spark ignition device was activated, the area around the ignition point released a significant amount of thermal energy due to the influence of the electrical energy, igniting the combustible gas at the ignition point. Due to molecular diffusion, the temperature of the unburned gas rose, causing the combustion wave to continuously advance into the unburned gas and leading to deflagration inside the pipeline. The flame evolved hemispherically from the point of the highest thermal energy at the ignition point, and it became finger-shaped under the compression of the wall as it reached the wall. At this time, deflagration still occurred. Upon reaching the front of the first obstacle, the flame bent upward due to the compression effect of the shock wave, causing the temperature of the unburned gas to rise and to trigger chemical reactions, accelerating the flame as it flowed over the obstacle. After passing the first obstacle, flame backflow formed in the narrow space behind it, and a vortex structure formed slightly further back. By comparing the experimental image at 30.4 ms with the simulation image at 30 ms, it was found that the simulation also captured a certain degree of outward diffusion of the flame after it passed the first obstacle, which was consistent with the actual situation.

Figure 6 shows that the experimental and simulated pressure curves fit extremely well. When the pressure wave reached the pipeline outlet, the polyethylene film

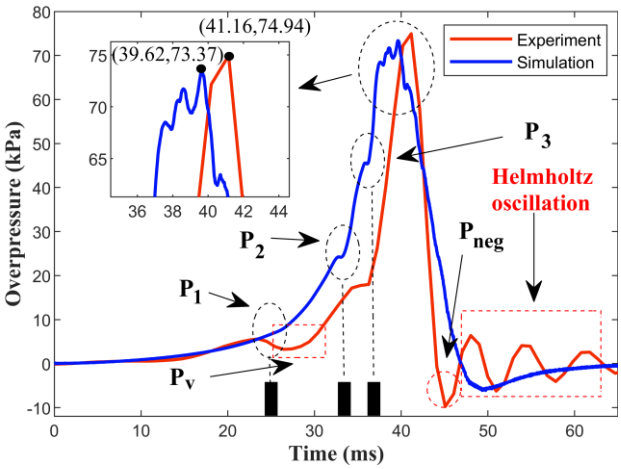

Fig. 6 Real and simulated pressure curves

ruptured, causing internal pressure fluctuations and a brief drop in pressure, forming the concave curve at point Pv in Fig. 6. This phenomenon has been extensively described and discussed in many previous studies (Ponizy & Leyer, 1999; Fakandu et al., 2015; Cao et al., 2018; Li et al., 2021). However, due to the simulation conditions, the presence of the polyethylene film could not be replicated, resulting in the absence of this special phenomenon in the simulation curve. Additionally, since the pipeline was set to adiabatic and no-slip conditions in the solver, the energy and waves of the flame propagation did not dissipate and were not obstructed during the simulation. In contrast, the actual pipeline was constructed of ordinary Q235-A steel plates, which have a certain surface roughness and absorb some heat. As a result, when the flame reached 200 mm and began to accelerate, the pressure increase in the simulation occurred 1–2 ms earlier than in the experiment. By combining the analysis results with flame propagation images, it was found that the simulation curve accurately captured the pressure fluctuations when the flame flowed over the obstacles; however, this specific stage

phenomenon was not detected in the experiment due to sensor precision limitations. When the flame exited the pipeline, the internal pressure reached its peak. When the deflagration reaction was over, the experimental curve oscillated and gradually weakened until it smoothed out near 0. This is known as Helmholtz oscillation (Fang et al., 2020). This is a phenomenon that develops due to the actual deflagration end section where there are sharp pressure fluctuations inside and outside the outlet and air repeatedly enters and exits in the vicinity, which leads to self-excited oscillation of the system.

The simulated pressure curve clearly records the subtle pressure changes as the flame reaches each obstacle (points P1, P2, and P3 in Fig. 6). When the flame reached the obstacles, it was compressed and deformed, releasing greater energy and making the pressure curve steeper. However, in the experiment, due to sensor precision limitations, the sampling interval was greater than the frequency of the pressure changes during the rapid response period, so it failed to capture the subtle changes during the pressure rise period. The pressure peak at point P3 exhibits small-scale fluctuations because the flame front became highly fragmented after being disturbed by the first two obstacles in the simulation. The flame propagation direction became less focused and was reflected after touching the wall, leading to continuous small-scale pressure fluctuations at the peak. The difference between the simulated and actual pressure was within 2.1%, which is reasonable.

4. RESULTS AND DISCUSSION

4.1 Analysis of Flame Propagation Behavior

Figure 7 displays flame progression diagrams for various cases obtained from the simulation. From 10 ms and 16 ms, in all four cases, after the ignition, the surrounding area entered a slow combustion state. Due to the effects of heat conduction and molecular diffusion, the temperature of a wider area of unburned mixed gas increased and entered the reaction zone, causing chemical reactions and continuously pushing the combustion wave into the unburned mixed gas. The type of obstacle did not affect the shape of the flame before the flame touched the obstacle.

Based on Figs 7(a) and 7(b), at 25 ms, when the flame was about to touch the obstacle, turbulence caused the flame to bend and stretch, and the intensity of the deflagration reaction increased, accelerating the flame. At this time, the flame in Fig. 7(b) developed ahead of the flame in Fig. 7(a), indicating that the continuous obstacle plates further stimulated the flame propagation process compared to the single plate obstacles. In Figs 7(a) and 7(b), at 29, 30, and 32 ms, after the flame crossed the continuous obstacle plates, the flame's stretching degree became more pronounced, the surface area of the flame front increased, and the heat generated by the combustion could heat a larger area of the adjacent unburned regions through conduction, speeding up the chemical reaction. This outcome produced a smaller cavity area within the flame backflow structure. As can be seen from the flame cavities between the first and second obstacles in Figs 7(a) and 7(b), after 33 ms, the cavity area in Fig.e 7(b) was larger. This is because the total energy of the combustible gas in the pipeline was constant, and this area was relatively closed. The continuous obstacle plates further intensified the deflagration reaction. Due to the inertia of the flame in the direction of the outlet, it quickly passed through this area, resulting in insufficient gas chemical reactions in the area behind the continuous obstacle board.

As can be seen from Figs 7(a) and 7(c), the flame trend upstream of the continuous obstacle plates was almost identical to the cases with single plate obstacles. As can be seen from Fig. 7(c), when the flame front reached the middle of the pipeline, at 32 ms, the flame front thickness increased. This means that when crossing the continuous obstacle plates, the chemical reaction at the front became more intense, undoubtedly indicating that the continuous obstacle plates further stimulated the flame trend. This is consistent with the pattern when the continuous obstacle plates were placed closer to the ignitor. Additionally, as can be seen from Fig. 7(c), at 34 ms, the flame mass was thicker compared to the other cases, the flame front surface area was larger, and the flame backflow cavity was is smaller, also reflecting a more intense chemical reaction behind the continuous obstacle plates. As can be seen from Fig. 7(d), at 36 ms, near the outlet, the flame mass behind the continuous obstacle plates was thicker and more pronounced, and the cavity formed was smaller, which is consistent with the above analysis.

At 35 ms, 36 ms, and 37 ms, in the cases shown Figs 7(a), 7(c), and 7(d), the flame structures between the first and second obstacles are almost identical, indicating that the continuous obstacle plates downstream did not affect the flame behavior upstream. By comparing the rectangular area in Fig. 7(b) with other cases, it was found that the impact of the continuous obstacle plates on the flame behavior was obvious, and there were more pronounced disturbances in the flame structure behind the continuous obstacle plates. By comparing the elliptical area in Fig. 7(c) with the other cases, we found that the flame structures were significantly different. However, unlike the rectangular area, a secondary shock wave impacted the downstream area. This occurred because when the flame crossed the second obstacle, it moved quickly and was disturbed by the continuous obstacle plates, resulting in less time for the combustible gas to undergo a chemical reaction. When the subsequent compression wave arrived, the chemical reaction in this area became active again, leading to the development of a secondary flame front structure towards the downstream area. By comparing the polygonal area in Fig. 7(d) with the other cases, it was observed that a secondary flame front formed. In contrast, when no continuous obstacle plates were present or they were placed closest to the ignitor, no secondary flame structure was formed. This is because the flame fully developed upstream of the obstacle, and when it reached the first obstacle, its speed was not high enough, allowing more time for the chemical reaction to occur, and thus, a secondary flame did not form.

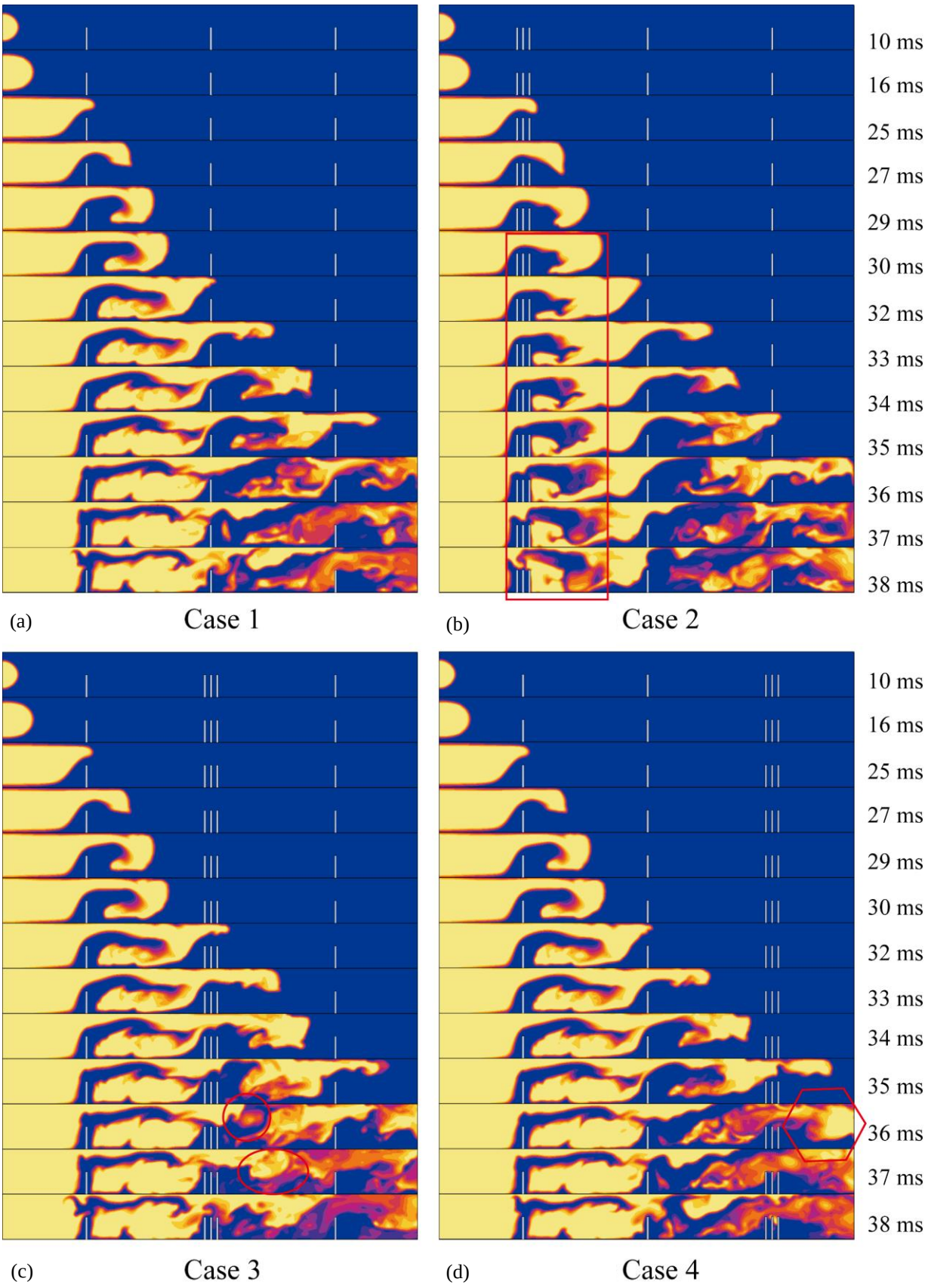

Fig. 7 Comparison of flame in four cases

By comparing the shape of the flame at each key node in the four cases, we found that the continuous obstacle plates could stimulate the flame trend and increase the intensity of the local deflagration reaction. As the distance between the continuous obstacle plates and the ignitor increased, the increasingly fragmented flame mass experienced a stronger initial impact. This is shown in Fig. 7, in which the flame still exhibits a certain

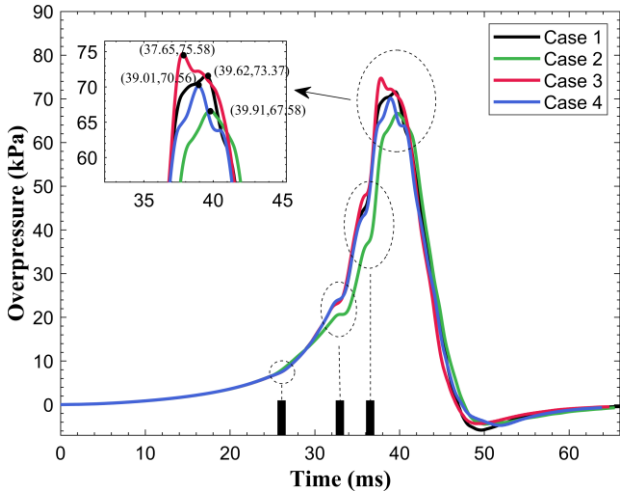

Fig. 8 Comparison of pressure characteristics in the different cases

regular structure in the later stages in cases 1 and 2, while the flame mass is located in the latter half of the pipeline in cases 3 and 4. When the continuous obstacle plates were placed too close together, the flame backflow trend was impacted by the upstream flame, forming a flame backflow vortex slightly further downstream. When placed at a moderate distance, the flame already exhibited a certain initial high-speed movement, forming a brief flame backflow slightly above the back side of the continuous obstacle plates. When the continuous obstacle plates were placed near the vent, the upstream flame weakened and diffused, exhibited irregularity developed chaotically slightly above the continuous obstacle plates, and diffused until it touched the wall and dissipated. The tertiary backflow formed offset part of the upstream flame's power to some extent.

4.2 Characteristics of Pressure Changes During Flame Propagation

Figure 8 compares the pressure data for the four cases. In the 0–22 ms segment, the pressure rise trends were consistent across all four cases. When the flame front touched the obstacle, the flame was compressed, deformed, and bent upwards due to the obstacle, further intensifying the chemical reaction in the area near the obstacle. This caused the pressure value to start rising rapidly. The pressure rise was the largest in case 2 (green line) due to the greater disturbances caused by the continuous obstacle plate on the flame, shock wave, and rear compression wave, which led to a more intense chemical reaction near the obstacle. Consequently, the amplitude of the pressure variation became more distinct compared to the other cases. As the deflagration process continued, the difference in the impacts of the continuous obstacle plates and single plate obstacles on the upstream flame and overpressure became more pronounced. Around 33 ms, the pressure rise potential was lower in case 2 than in the other cases, suggesting that placing the continuous obstacle plate 200 mm from the ignitor exhausted the deflagration reaction potential. This is reflected in the lower pressure values at the same moment at the second obstacle and in the downstream regions. However, regarding the speed of the flame and the explosion process moving forward along the pipeline, there was no significant difference between the two types of obstacles. When the continuous obstacle plate was placed at 500 mm, the pressure changes before and after the flame crosses the second obstacle differed from those in the other three cases. Due to the complexity of the continuous obstacle plate, the amplitude of the disturbance on the flame process as it crossed the obstacle was greater and more chaotic, increasing the area of the flame front and more fully contacting with the unburned gas, thus making the chemical reaction more active. This resulted in a stronger deflagration reaction, which is reflected in the higher pressure values when the continuous obstacle plate was placed at 500 mm. As the flame advanced to the upstream side of the next obstacle, the overpressure peak was markedly different compared to the other scenarios. When the flame process progressed and crossed the 800 mm obstacle, the pressure values increased significantly in all four cases. The differences were more pronounced, and the peak pressure was reached. The pressure rise in case 3 was the most significant. This is because the flame became more fragmented after being disturbed by the continuous obstacle plate at 500 mm, and in its continued development, the flame encountered a greater amount of unburned gas and oxygen, causing a more intense deflagration reaction and increasing the overpressure. The pressure rise in case 2 was the weakest due to the suppression effect at the first obstacle, resulting in overall weaker development.

Table 3 presents the peak pressure values and arrival time information for the four cases. In Table 3, P_{max} is the peak pressure, TG_1 is the time gap, which is the difference in the arrival time of the peak pressure relative to case 1, T_{max_1} is the time of the peak pressure arrival, and GR_1 is the growth rate, which is the increase in the peak pressure relative to case 1. It can be observed that when continuous obstacles were placed 200 mm, the peak pressure significantly decreased by 8.57% compared to the case with three single obstacles, reflecting the strong suppression of the detonation process by the continuous obstacles. The arrival time of the peak pressure exhibited little variation, and was slightly slower (by 0.29 ms) compared to case 1. When continuous obstacles were placed 500 mm from the ignition source, GR_1 reached 2.92%, the only positive

Table 3 Peak pressure and arrival time information for the four cases

Case	P_{max} (kPa)	GR_1 (%)	T_{max_1} (ms)	TG_1 (ms)
Case 1	73.37	0	39.62	0
Case 2	67.58	−8.57	39.91	0.29
Case 3	75.58	2.92	37.65	−1.97
Case 4	70.56	−3.98	39.01	−0.61

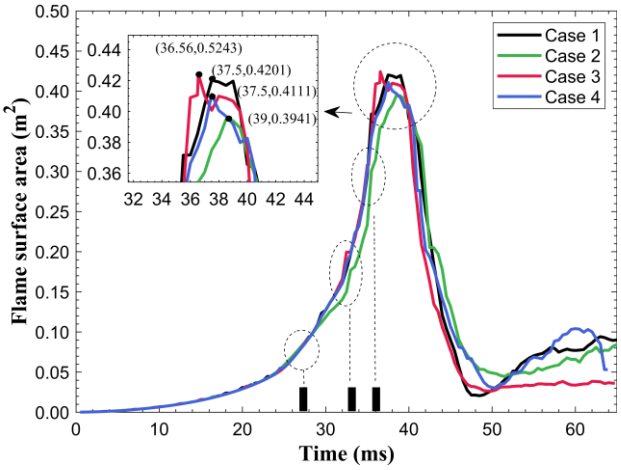

Fig. 9 Diagram showing the surface area of the flame

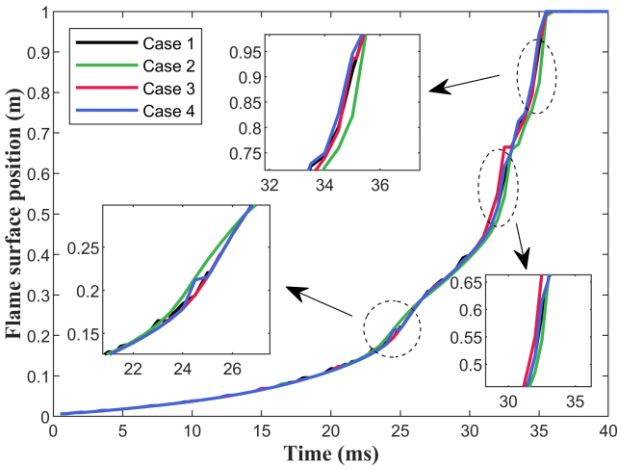

Fig. 10 Diagram showing the position of the flame front

value, indicating that the continuous obstacles at this distance stimulated the detonation process within the pipeline. At 800 mm from the ignition source, the peak pressure dropped by 3.98%, suggesting some suppression effect. However, since this location was farther from the ignition point, the flame behavior and pressure propagation had already developed sufficiently in the upstream area, resulting in relatively minor restrictions on the pressure compared to case 2.

After reaching the pressure peak, the pressure values at the same moment also differed significantly. Specifically, the pressure value was highest in case 2, which was suppressed in the first half; and the pressure value was lowest in case 3, which experienced the most significant deflagration in the first half. This is because given the constant amount of combustible gas and oxidant in the pipeline, the more intense the energy release was, the shorter the process was, and a relatively stable deflagration process lasted longer.

4.3 Coupling Characteristics of the Position and Area of the Flame Front

Figure 9 compares the flame surface area data for each case. By observing the key change nodes (circled in Fig. 9), when the continuous obstacle plate was placed at 200 mm, it more effectively disturbed the flame structure, causing the flame to break more fully and the flame surface area to develop earlier compared to the other cases. However, as the deflagration process continued, after the flame crossed the barrier at 200 mm, in case 2, the flame area gradually no longer led. During the initial process of the flame being stretched and bent by the obstacle at 200 mm, the complexity of the continuous obstacle plate briefly stimulated the flame fragmentation, making the chemical reaction in this area more active. However, due to insufficient flame development, in the subsequent development, the flame gradually appeared weaker than in the other cases, which was reflected in the entire process before the area reached the peak value. The flame area was maintained relatively longer than in the other cases, which was consistent with the pressure development in this case. When the continuous obstacle plate was placed at 500 mm, it slightly delayed the development of the flame area, and then played the most positive role in the expansion of the flame area. This is reflected in Fig. 9 as a sharp increase in the area curve, followed by more rapid development at a steeper angle. When the continuous obstacle plate was placed at 500 mm, the area values further increased in all of the cases, with more pronounced differences, and reached the peak value. In the latter half of the deflagration reaction, the flame area was smallest in case 3 and largest in case 2 at the same moment. This is because in the first half, case 3 had the most active overall chemical reaction, consuming more combustible gas and causing a faster rate of pressure increase and a greater peak pressure. Due to suppression, case 2 had the least active chemical reaction, resulting in a slower rate of increase of the pressure and the lowest peak pressure. However, this made the chemical reaction in the latter half of the deflagration reaction more active in case 2. As can be seen from Fig. 9, the peak flame surface area was the largest in case 3. The results of each case demonstrate that the flame surface area development aligned closely with the pressure curve, indicating a coupling relationship.

Figure 10 compares the flame surface position data for each case. The development trend of the position of the flame front and the time it took to reach the pipeline's outlet were relatively consistent across all four cases, and there were only slight differences when the flame crossed the obstacles. Based on the time nodes of the flame front as it crossed the obstacles (circled in Fig. 9), when the continuous obstacle plate was placed at 200 mm, it could more effectively stimulate the local advancement speed of the flame front. After bending and stretching, the flame front broke above the continuous obstacle plate, This is reflected by the fact that the position of the flame front (green line in Fig. 9) was further ahead at the same moment. This indicates that in case 2, the flame accelerated downstream at this moment. From the previous analysis, it is known that in case 2, the flame overpressure was suppressed and the deflagration behavior was not as sufficient as in the other cases, leading to a weaker rise in the surface area of the flame and resulting in the longest time lag at the same moment

Table 4 Information about the maximum area of the flame and the arrival time for the four cases

Case	A_{max} (m^2)	GR_2 (%)	T_{max_2} (ms)	TG_2 (ms)
Case 1	0.4201	0	37.5	0
Case 2	0.3941	−6.60	39	1.5
Case 3	0.5243	19.87	36.56	−0.9
Case 4	0.4111	−2.19	37.5	0

after crossing the obstacle. When the flame front reached the second obstacle, the chemical reaction at this position was most active in case 3, causing the position of the flame front to quickly reach the lead position. When the deflagration process continued between the second and third obstacles, in case 2, the chemical reaction was active, absorbing a certain amount of combustible gas slightly downstream of the obstacle. This results in insufficient combustible gas slightly downstream of the second obstacle and relatively weaker chemical reaction activity, causing the flame front position to lag. The changes in case 4 at the third obstacle are similar to the above analysis. It can be seen that the type of obstacle affects the local changes in the flame front position, but given the constant combustible material and pipeline length, the time required for the front face to reach the exit is almost constant.

Table 4 displays the maximum flame area and arrival time information for each condition. A_{max} represents the maximum flame area, GR_2 is the growth rate relative to the maximum flame area in case 1, T_{max_2} is the arrival time of the maximum flame area, and TG_2 is the time gap in the arrival time compared to case 1. It is evident that when the continuous obstacles were located 200 mm from the ignition, the maximum flame area significantly decreased by 6.6% compared to the case with three single obstacles, indicating that these continuous obstacles impeded the diffusion of the flame area. When the obstacles were positioned 500 mm from the ignition, the maximum flame area increased dramatically (by 19.87%), allowing for better contact between the flame and the oxidizer, thereby enhancing the detonation reaction. This condition (case 3) had the only positive maximum flame area among the three cases with continuous obstacles. However, when the continuous obstacles were placed 800 mm, the maximum flame area slightly decreased (by 2.19%), which was the smallest absolute value among the three groups. This was because the distance from the ignition caused the flame to develop fully upstream, resulting in a reduction in the influence on the flame behavior compared to when the obstacles were positioned closer.

By comparing the peak pressure arrival times in Table 3, it was found that the arrival time of the maximum flame area was slightly earlier than that of the peak pressure in all four cases. When the flame area reached the maximum value, it facilitated better contact between the flame and the oxidizer, thus stimulating the generation of the peak pressure.

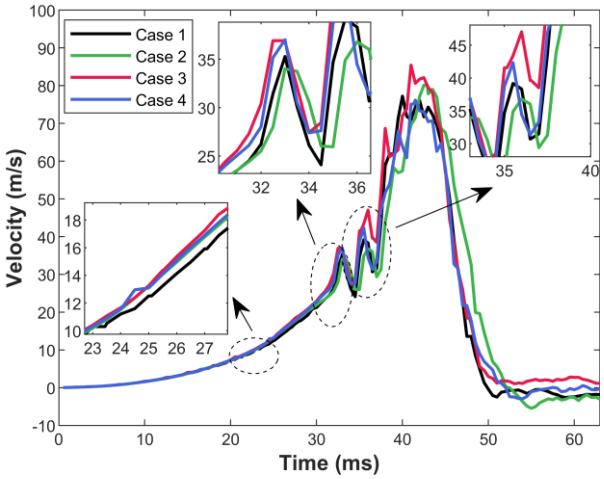

Fig. 11 Flame velocity field development

4.4 Flame Velocity Field Development Properties

Figure 11 illustrates the development of the flame velocity field. It can be seen that after 20 ms, when the flame crossed the obstacle at 200 mm, in all four cases, the velocity began to accelerate. As the flame further advanced to the obstacle at 500 mm, indicated by the elliptical area in Fig. 11, the flame continued to rise due to stimulation from the obstacle. Based on this and the flame behavior shown in Fig. 7, the flame was pushed upwards. When the flame touched the wall, it rebounded, which disrupted the flame propagation path to some extent. This is reflected in the velocity curve as a local minimum velocity value within the ellipse (Fig. 11).

Table 5 presents the maximum flame velocities at the 500 mm and 800 mm obstacles. V_{max} is the maximum velocity at a specific point, and GR_3 is the growth rate, which indicated the increase in the maximum velocity compared to case 1 at that moment. It was found that in case 2, when the flame reached the 500 mm point, the maximum velocity was 34 m/s, the only negative value among the three cases with continuous obstacles, reflecting a decrease of 3.76%. This suggests that the continuous obstacles placed at 200 mm affected the sustained development of the downstream flame and suppressed the detonation process.

Table 5 Maximum flame velocities at the 500 mm and 800 mm obstacles

Case	V_{max_500mm} (m/s)	GR_3 (%)	V_{max_800mm} (m/s)	GR_3 (%)
Case 1	35.28	0.00	39.16	0.00
Case 2	34.00	−3.76	36.80	−6.41
Case 3	36.92	4.44	47.04	16.75
Case 4	37.02	4.70	42.33	7.49

By further examining cases 3 and 4, the maximum velocities were found to be 36.92 m/s and 37.02 m/s, with increases of 4.44% and 4.70% compared to the maximum velocities of case 1. Regarding the maximum velocity of the flame at the 800 mm obstacle, in case 2, the maximum velocity was 36.80 m/s, which further expanded the decrease compared to the single obstacle configuration, with a drop of 6.41%. This indicates that the suppressive effect of the continuous obstacle placed at 200 mm on the detonation process increased as the detonation progressed within the pipeline.

In contrast, in cases 3 and 4, the flame velocities were 47.04 m/s and 42.33 m/s, i.e., increases of 16.75% and 7.49% compared to the flame velocities of case 1. The difference in these increases was significant, indicating that in case 3, the continuous obstacle placed at 500 mm enhanced the detonation process in the local interval between 500 mm and 800 mm, resulting in a substantial increase in the velocity of the flame at this moment.

Through analysis of the flame velocity development graph, it was found that the influence of the continuous obstacles on the velocity of the flame was primarily evident after the flame crossed the obstacles. The continuous obstacle at 200 mm significantly suppressed the downstream flame velocity, while the obstacle at 500 mm notably stimulated an increase in the downstream flame velocity. As the detonation process continued, the differences in the flame velocities in these two cases and those with three single obstacles gradually increased.

4.5 Coupling Analysis of Vortex Generation and Flame Response in the Pipeline

Figure 12 displays superimposed images of the flame propagation, pressure changes, and flow field within the pipeline. The black lines represent the positions of the flame front, the white lines are the flow field lines, and the color gradient of the background indicates the changes in the pressure field. The presence of obstacles profoundly impacted the flame, flow field, and pressure, and the different types of obstacles and their positions greatly influenced the flow field. After the spark igniter was activated, the area around the ignition point became a source of heat and chemically active particles. The center of the flame supplied heat and active particles to the surrounding thin layer of unburned gas. The flame peak in the reaction zone spread rapidly outward in a hemispherical shape. The heat released from combustion caused the product volume to expand rapidly, increasing the surrounding pressure.

The flame's behavior and forward flow field propagation were disturbed by obstacles. At 25 ms, the flow field lines began to concentrate upward upstream of the obstacle, and the flame simultaneously bent and its surface became wrinkled. The pressure stratification at the obstacle was evident, and due to the blockage of the obstacle, the flame front did not directly impact it, resulting in a relatively low-pressure area behind and below the obstacle. This was caused by the further intensification of the deflagration reaction due to the broken flame and propagating streamlines. Notably, a backflow phenomenon occurred behind the obstacle. When the flame front crossed the first obstacle, the vortex field behind the continuous obstacle plate became denser and more compact. This is because the continuous obstacle plate was longer and had a discontinuous smooth surface compared to the single plate obstacle in the narrow local area above, which more effectively disturbed the flame's behavior and blocking pressure transmission, leading to more intense chemical reactions.

In all four cases, at 27 ms, the flame front had moved beyond the obstacle and had extended to the bottom of the pipeline. It eventually covered the entire cross-section once more. Due to the inertial forces exerted by the diffusion and the influence of the flow field, some of the flames turned and backflow occurred slightly behind the obstacle. The impact of the downstream second obstacle on the internal state was also evident. When the continuous obstacle plate was placed at 500 mm, this type of obstacle disturbed the flame front and flow field changes more effectively than the single plate obstacle, causing the flame to break more extensively above the obstacle, exposing a larger surface area, and making full contact with the surrounding combustible gas, which resulted in very active surrounding chemical reactions. This led to a more intense deflagration reaction compared to the single plate obstacles.

As the flame front continued to advance, at 34 ms, the vortex field behind the obstacle at 500 mm in case 3 was the densest. This further confirms that the continuous obstacle plates more effectively disturbed the flame front and flow field changes. Case 2 yielded the second strongest vortex field intensity, and the backflow range was broader in this case. This is because after the flame crossed the continuous obstacle plate at 200 mm, it experienced more severe disturbances, causing the surface to break more and the surrounding backflow to be more dispersed. When the flame reached the third obstacle, at 35 ms, in all of the cases, except for case 3, flame backflow formed upstream of the third obstacle. The tightness of the lines can be ranked as follows: case 1 > case 4 > case 2. Additionally, the pressure can be ranked from highest to lowest as follows: case 3 > case 1 > case 4 > case 2. It can be seen that the magnitude of the pressure was directly proportional to whether or not the backflow was tight. When there was no backflow, such as in case 3, when the continuous obstacle plate was placed at 500 mm, the flame crossed the continuous obstacle plate smoothly towards the pipeline's outlet, significantly increasing the pressure. In the cases with backflow, such as case 1, case 4, and case 2, some of the energy in the backflow area was dissipated, preventing higher pressure peaks from being generated. The more dispersed the backflow area was, the smaller the increase in the pressure was. The continuous obstacle plates in cases 2 and 4 were more likely to cause backflow, resulting in lower pressure peaks compared to the single plate obstacle cases. This shows that the position and type of obstacles had different effects on the vortex generation and influenced the flame response, causing different pressure field changes. It Thus, it can be concluded that placing continuous obstacle plates 500

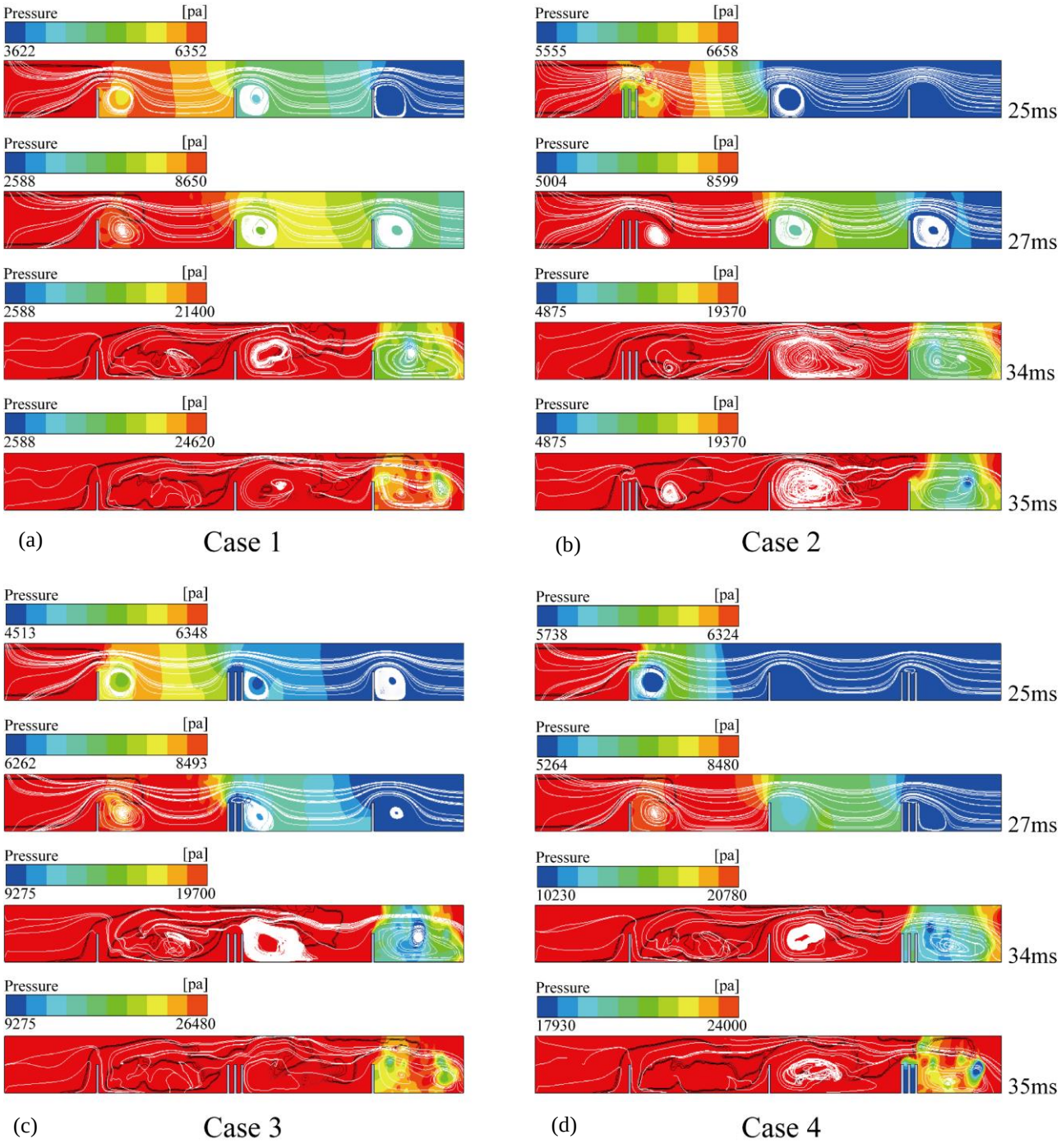

Fig. 12 Flow field distribution at key nodes in the four cases

mm from the ignitor positively affects the pressure peak, while placing them at 200 mm and 800 mm negatively affects the pressure peak.

5. CONCLUSIONS

For underground pipeline spaces containing densely arranged equipment groups or structures, the characteristics of deflagration reactions significantly differ from those in conventional pipeline spaces. In this study, we simplified the groups of equipment and structures as a continuous obstacle plate to study the characteristics of the flame and the pressure changes related to the characteristics of the deflagration process. The following main conclusions were drawn.

(1) When continuous obstacle plates are placed at 500 mm and 800 mm from the ignition point, secondary flame fronts form. The fully fragmented flame front quickly crosses the continuous obstacle plates, causing insufficient chemical reactions in this area due to the short time of the reaction. When subsequent compression waves arrive, the chemical reaction in this area reactivates, leading to the development of secondary flame front structures towards the downstream area.

(2) Compared to ordinary single plate obstacles, continuous obstacle plates more effectively influence the

local development of the position of the flame front near the obstacles, stimulating a brief rapid rise in the flame front. However, regardless of the type of obstacle and the placement configuration, the flame front's travel time to the pipeline outlet is almost identical. Additionally, the placement of continuous obstacles influences the downstream velocity changes. When the obstacle is positioned at 200 mm, the flame velocities at 500 mm and 800 mm decrease by 3.76% and 6.41%, respectively, compared to the scenario with three single obstacles. Conversely, when continuous obstacles are placed at 500 mm, the flame velocity at 800 mm significantly increases by 16.75% compared to the scenario with three single obstacles.

(3) Due to the structural complexity of continuous obstacles, the flow field experiences more variations as it flows around them, causing greater disturbances of the flame development. This is particularly evident in the formation of different backflow phenomena below the obstacles, which accelerates the speed of the flame passage and results in more pronounced pressure changes in the surrounding areas. The degree of backflow diffusion affects the peak pressure. When continuous obstacles are placed 200 mm and 800 mm from the ignition point, they negatively impact the peak pressure and maximum flame area, resulting in pressures of 67.58 kPa and 70.56 kPa, i.e., the peak pressure reductions of 8.57% and 3.98% compared to the case with three single obstacles. The maximum flame areas at 200 mm and 800 mm are 0.3941 m^2 and 0.4111 m^2, decreases of 6.60% and 2.19%, respectively. However, when continuous obstacles are positioned 500 mm from the ignition source, they positively influence the peak pressure and maximum flame area, resulting in a peak pressure of 75.58 kPa, an increase of 2.92% compared to three single obstacles, and a maximum flame area of 0.5243 m^2, i.e., an increase of 19.87%.

ACKNOWLEDGEMENTS

This work was supported by the Basic Public Welfare Research Project of Zhejiang Province (Grant No. LGF22E040002).

We thank LetPub (www.letpub.com.cn) for its linguistic assistance during the preparation of this manuscript.

CONFLICT OF INTEREST

The authors declare that they have no known competing financial interests or personal relationships that could have appeared to influence the work reported in this paper.

AUTHORS CONTRIBUTION

Xiaojun Shao: Methodology, Investigation, Software, Writing – original draft. **Bin Hao:** Writing – Review & editing, Supervision. **Jianfeng Gao:** Funding Acquisition, Resources. **Bingjian Ai:** Data Curation, Formal Analysis. **Yanan Han:** Experimentation. **Yang Wu:** Experimentation. **Bingang Guo:** Formal Analysis.

REFERENCES

Ajrash, M. J., Zanganeh, J., & Moghtaderi, B. (2017). Deflagration of premixed methane-air in a large scale detonation tube. *Process Safety and Environmental Protection, 109*, 374-386. https://doi.org/10.1016/j.psep.2017.03.035

Bao, Q., Fang, Q., Yang, S. G., Zhang, Y. D., Xiang, H. B., Chen, L., & Li, Z. (2016). Experimental investigation on the deflagration load under unconfined methane-air explosions. *Fuel, 185*, 565-576. https://doi.org/10.1016/j.fuel.2016.07.126

Bu, F. X., Liu, Y., Liu, Y. B., Xu, Z., Chen, S. Q., Jiang, M. H., & Guan, B. (2021). Leakage diffusion characteristics and harmful boundary analysis of buried natural gas pipeline under multiple working conditions. *Journal of Natural Gas Science and Engineering, 94*. https://doi.org/10.1016/j.jngse.2021.104047

Cao, Y., Li, B., & Gao, K. H. (2018). Pressure characteristics during vented explosion of ethylene-air mixtures in a square vessel. *Energy, 151*, 26-32. https://doi.org/10.1016/j.energy.2018.03.012

Chen, Y., Li, Z. T., Ji, C., & Liu, X. Y. (2020). Effects of hydrogen concentration, non-homogenous mixtures and obstacles on vented deflagrations of hydrogen-air mixtures in a 27 m3 chamber. *International Journal of Hydrogen Energy, 45*(11), 7199-7209. https://doi.org/10.1016/j.ijhydene.2019.11.082

Cui, G., Li, Z. L., & Yang, C. (2016). Experimental study of flammability limits of methane/air mixtures at low temperatures and elevated pressures. *Fuel, 181*, 1074-1080. https://doi.org/10.1016/j.fuel.2016.04.116

Debnath, P., & Pandey, K. M. (2024). Exergetic and Thermal performance analysis of liquid and gaseous fuel–air mixture in PDC using computational fluid dynamics. *Arabian Journal for Science and Engineering.* https://doi.org/10.1007/s13369-024-09319-5

Debnath, P., & Pandey, K. M. (2014). Effect of blockage ratio on detonation flame acceleration in pulse detonation combustor using CFD. *Applied Mechanics and Materials, 656*, 64-71. https://doi.org/10.4028/www.scientific.net/AMM.656.64

Debnath, P., Pandey, K., & Science, S. (2023). Numerical Investigation on detonation combustion waves of hydrogen-air mixture in pulse detonation combustor with blockage. *Advances in aircraft and spacecraft, 10*(3), 203-222. https://doi.org/10.12989/aas.2023.10.3.203

Fakandu, B. M., Andrews, G. E., & Phylaktou, H. N. (2015). Vent burst pressure effects on vented gas explosion reduced pressure. *Journal of Loss Prevention in the Process Industries, 36*, 429-438. https://doi.org/10.1016/j.jlp.2015.02.005

Fang, Z. L., Zeng, F. D., Xiong, T., Wei, W., Jiang, P., Wu, Q., Wang, Y. S., & Fei, Y. X. (2020). Large eddy simulation of self-excited oscillation inside Helmholtz oscillator. *International Journal of Multiphase Flow*, *126*. https://doi.org/10.1016/j.ijmultiphaseflow.2020.103253

Hong, Y. D., Lin, B. Q., & Zhu, C. J. (2016). Premixed methane/air gas deflagration simulations in closed-end and open-end tubes. *International Journal of Spray and Combustion Dynamics*, *8*(4), 271-284. https://doi.org/10.1177/1756827716648640

Huang, L. J., Li, Z. F., Wang, Y., Zhang, L., Su, Y. L., Zhang, Z., & Ren, S. R. (2021). Experimental assessment on the explosion pressure of CH4-Air mixtures at flammability limits under high pressure and temperature conditions. *Fuel*, *299*. https://doi.org/10.1016/j.fuel.2021.120868

Huang, L. J., Wang, Y., Pei, S. F., Cui, G. D., Zhang, L., Ren, S. R., Zhang, Z., & Wang, N. R. (2019). Effect of elevated pressure on the explosion and flammability limits of methane-air mixtures. *Energy*, *186*. https://doi.org/10.1016/j.energy.2019.07.170

Huang, L. J., Wang, Y., Zhang, L., Su, Y. L., Zhang, Z., & Ren, S. R. (2022). Influence of pressure on the flammability limits and explosion pressure of ethane/propane-air mixtures in a cylinder vessel. *Journal of Loss Prevention in the Process Industries*, *74*. https://doi.org/10.1016/j.jlp.2021.104638

Huo, Y., Zou, G. W., Dong, H., & Cheng, F. M. (2022). Propagation characteristics of turbulent deflagration in horizontal tunnel with lateral liquefied petroleum gas concentration variations. *Tunnelling and Underground Space Technology*, *124*. https://doi.org/10.1016/j.tust.2022.104477

Li, G., Wu, J., Wang, S., Bai, J., Wu, D., & Qi, S. (2021). Effects of gas concentration and obstacle location on overpressure and flame propagation characteristics of hydrocarbon fuel-air explosion in a semi-confined pipe. *Fuel*, *285*. https://doi.org/10.1016/j.fuel.2020.119268

Li, P. L., Liu, Z. Y., Li, M. Z., Huang, P., Zhao, Y., Li, X., & Jiang, S. K. (2019). Experimental study on the flammability limits of natural gas/air mixtures at elevated pressures and temperatures. *Fuel*, *256*. https://doi.org/10.1016/j.fuel.2019.115950

Liu, J., & Wang, H. (2022). Machine learning assisted modeling of mixing timescale for LES/PDF of high-Karlovitz turbulent premixed combustion. *Combustion and Flame*, *238*, 111895. https://doi.org/10.1016/j.combustflame.2021.111895

Liu, X. J., Xu, Z. D., Sun, B., Liu, X. Y., & Xu, D. J. (2024). Spatiotemporal state assessment for the underground pipe gallery: Physical model and experimental verification. *Tunnelling and Underground Space Technology*, *143*. https://doi.org/10.1016/j.tust.2023.105474

Liu, Z. R., Li, X. X., Li, M., & Xiao, H. H. (2023). Flame acceleration and DDT in a channel with fence-type obstacles: Effect of obstacle shape and arrangement. *Proceedings of the Combustion Institute*, *39*(3), 2787-2796. https://doi.org/10.1016/j.proci.2022.08.046

Lv, X. S., Zheng, L. G., Zhang, Y. G., Yu, M. G., & Su, Y. (2016). Combined effects of obstacle position and equivalence ratio on overpressure of premixed hydrogen-air explosion. *International Journal of Hydrogen Energy*, *41*(39), 17740-17749. https://doi.org/10.1016/j.ijhydene.2016.07.263

Mei, Y., Shuai, J., Li, Y. T., Zhou, N., Ren, W., & Ren, F. (2023). Flame acceleration process of premixed hydrogen in confined space with different obstacle shapes. *Fuel*, *334*, 14. https://doi.org/10.1016/j.fuel.2022.126624

Metghalchi, M., & Keck, J. (1980). Laminar burning velocity of propane-air mixtures at high temperature and pressure. *Combustion and Flame*, *38*, 143-154. https://doi.org/10.1016/0010-2180(80)90046-2

Na'inna, A. M., Somuano, G. B., Phylaktou, H. N., & Andrews, G. E. (2015). Flame acceleration in tube explosions with up to three flat-bar obstacles with variable obstacle separation distance. *Journal of Loss Prevention in the Process Industries*, *38*, 119-124. https://doi.org/10.1016/j.jlp.2015.08.009

Nicoud, F., & Ducros, F. (1999). Subgrid-scale stress modelling based on the square of the velocity gradient tensor. *Flow, turbulence and Combustion*, *62*(3), 183-200. https://doi.org/10.1023/a:1009995426001

Pan, C., Wang, X., Sun, H., Zhu, X., Zhao, J., Fan, H., & Liu, Y. J. F. (2022). Large-eddy simulation and experimental study on effects of single-dual sparks positions on vented explosions in a channel. *Fuel*, *322*, 124282. https://doi.org/10.1016/j.fuel.2022.124282

Patankar, S. V. (1980). *Numerical heat transfer and fluid flow*. Hemisphere Publ. 58, 288. https://doi.org/10.1201/9781482234213

Ponizy, B., & Leyer, J. (1999). Flame dynamics in a vented vessel connected to a duct: 1. Mechanism of vessel-duct interaction. *Combustion and Flame*, *116*(1-2), 259-271. https://doi.org/10.1016/S0010-2180(98)00038-8

Qin, Y., & Chen, X. W. (2021). Flame propagation of premixed hydrogen-air explosion in a closed duct with obstacles. *International Journal of Hydrogen Energy*, *46*(2), 2684-2701. https://doi.org/10.1016/j.ijhydene.2020.10.097

Saeid, M. H. S., Khadem, J., & Emami, S. (2021). Numerical investigation of the mechanism behind the deflagration to detonation transition in homogeneous and inhomogeneous mixtures of H2-

air in an obstructed channel. *International Journal of Hydrogen Energy*, *46*(41), 21657-21671. https://doi.org/10.1016/j.ijhydene.2021.04.006

Shen, X. B., Zhang, B., Zhang, X. L., & Xiu, G. L. (2017). Explosion characteristics of methane-ethane mixtures in air. *Journal of Loss Prevention in the Process Industries*, *45*, 102-107. https://doi.org/10.1016/j.jlp.2016.11.012

Wan, H. W., Wen, Y. Q., & Zhang, Q. (2023). Flame behaviors and explosion characteristics of two-phase propylene oxide/air mixture under different ambient pressures. *Process Safety Progress*, *42*(1), 126-140. https://doi.org/10.1002/prs.12429

Wang, Q., Luo, X. J., Wang, C. J., Liu, Y., Zhou, P. G., & Li, B. (2022). Experimental study on external explosion for vented hydrogen deflagration in a rectangular tube with different vent coefficients. *Process Safety and Environmental Protection*, *158*, 331-339. https://doi.org/10.1016/j.psep.2021.12.002

Zimont, V., & Battaglia, V. (2006). Joint RANS/LES approach to premixed flame modelling in the context of the TFC combustion model. *Flow, Turbulence and Combustion*, *77*(1), 305-331. https://doi.org/10.1007/s10494-006-9048-0